Sub-Pixel Position Sensing for Pixelated, 3-D Position Sensitive, Wide Band-Gap, Semiconductor, Gamma-Ray Detectors

Yuefeng Zhu, Stephen E. Anderson, and Zhong He, *Member, IEEE*

***Abstract*—This article presents a technique to improve the lateral position resolution of pixelated 3-D position sensitive, semiconductor detectors. Improvements in lateral position resolution allow for more precise Compton-imaging calculations, detector-response calibrations, and interaction-based corrections resulting in better spectroscopic and imaging performance. In pixelated detectors, the lateral position resolution of a gamma-ray interaction location is traditionally limited to the dimensions of the individual pixels that constitute an anode array. Sub-pixel position resolution is achieved through algorithms that compare the amount of transient charge induced on pixels that neighbor a charge-collecting pixel. Measurements of the charge induced on the non-collecting pixels are made through analysis of digitized preamplifier pulse waveforms using optimized digital signal processing algorithms. A 2.0 cm × 2.0 cm × 1.5 cm CdZnTe detector with a pixel pitch of 1.72 mm is used to demonstrate the sub-pixel position technique. A 100 μm tungsten collimator is used to verify the accuracy of the method. The measured sub-pixel position resolution is 230 μm at 662 keV. This result is consistent with the predicted value of 180 μm at 662 keV based on a detailed system simulation assuming 4 keV FWHM electronic noise.**

***Index Terms*—CdZnTe detector, sub-pixel resolution, 3-D position sensitive.**

I. Introduction

THE performance and imaging capability of CdZnTe (CZT) detectors have improved steadily over the past decade. Energy resolutions around 1% FWHM at 662 keV have been consistently demonstrated using large volume ($1.5 \times 1.5 \times 1.0$ cm^3 or $2.0 \times 2.0 \times 1.5$ cm^3) pixelated CZT detectors at university of Michigan. An energy resolution of 0.48% FWHM at 662 keV for single-pixel-triggered events (or single-pixel events as we call) has been measured on a $2.0 \times 2.0 \times 1.5$ cm^3 crystal using BNL readout ASIC system [1]. These Pixelated CZT detectors are capable of providing 3-D position information of gamma-ray interactions within one detector volume. It is a key performance parameter for Compton imaging applications. The lateral position resolution of CZT detectors using pixelated anodes is currently limited by the pixel pitch. In our present CZT detector configuration, each pixel pitch is 1.72 mm. As a comparison, our depth sensing-techniques provide an interaction-depth resolution of about 0.5 mm [1], much more precise than the pixel pitch. This relatively poor lateral position resolution limits the Compton image angular resolution to roughly 40 degrees FWHM using simple back-projection reconstruction [2].

Better position resolution is desired to improve the angular resolution of gamma-ray imaging reconstruction. A number of efforts have been made in the past decades to achieve position resolution better than the dimension of charge collecting electrodes in semiconductor detectors. Warburton [3], Burks *et al.* [4] and Williams *et al.* [5] proposed and demonstrated a method to obtain improved position resolution based on induced transient signals on non-charge-collecting electrodes in striped CdZnTe and HPGe detectors. Marks *et al.* [6], Vickersa and Chakrabarti [7] and Jakubek and Uher [8] studied several algorithms to achieve sub-pixel position resolution when an electron cloud is collected by several pixels in pixelated detectors. Narita *et al.* [9] showed the difference in the transient signals on neighboring non-charge-collecting pixels in pixelated CdZnTe detectors when the gamma-ray interaction position was changed. For our detectors, the pixel size of the anode is 1.72 cm as mentioned above. It is bigger than or similar as the electron cloud size in the energy range of 0 to 3 MeV, the dynamic range of our detector system [10]. Therefore, the charge-sharing sub-pixel position determination method discussed in [6]–[8] can't be applied. The transient signal method mentioned in [4], [5] is promising. As mentioned in [9], the induced transient signals on the neighbor pixels change with electron cloud location. However, since the area of a pixel in our detectors is much smaller than the area of the anode strip in [4], [5], the induced transient signals on the non-collecting electrodes are expected to be much smaller in our case. Therefore, it is challenging to implement the transient signal method in our pixelated detectors.

This article describes the first detailed study on a sub-pixel position calculation algorithm based on non-charge-collecting transient signals [4], [5] for pixelated CdZnTe detectors. First, a detailed simulation to generate the signal pulse waveforms expected from the detection system is presented. Next, several sub-pixel position calculation algorithms are proposed for single-pixel events, which, combined with results from simulations, provides the theoretical limit on the best achievable position resolution as a function of electronic noise and energy deposition. These simulation results are then compared with the exper-

Manuscript received August 18, 2010; revised December 18, 2010 and January 28, 2011; accepted March 12, 2011. Date of publication April 19, 2011; date of current version June 15, 2011. This work was supported in part by the Office of Nonproliferation Research and Development (NA-22) of the Department of Energy and in part by the Defense Threat Reduction Agency of the Department of Defense.

The authors are with the University of Michigan, Nuclear Engineering and Radiological Sciences Department, Ann Arbor, MI 48109 USA (e-mail: zhuyuef@umich.edu).

Digital Object Identifier 10.1109/TNS.2011.2132738

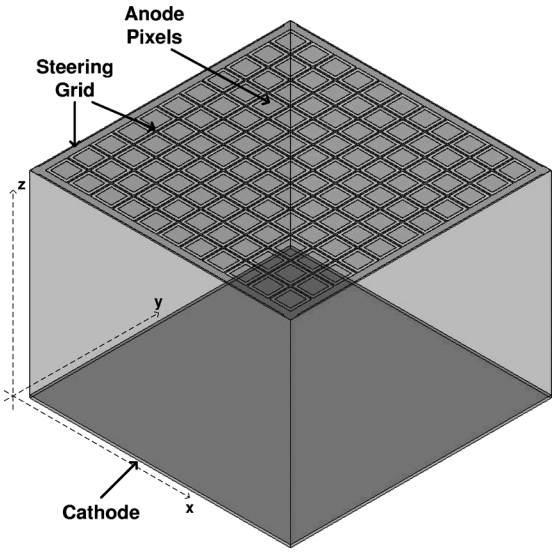

Fig. 1. An illustration of the pixelated CdZnTe detector used in this study.

imental data from a $2.0\ \text{cm} \times 2.0\ \text{cm} \times 1.5\ \text{cm}$ CZT detector irradiated with a ^{137}Cs 662 keV gamma-ray source collimated by a tungsten collimator with a 100 μm opening. The result validated the accuracy of the proposed sub-pixel calculation methods. Finally, a method for measuring sub-pixel positions for two-pixel triggered events (or two-pixel events as we call) is presented and discussed.

II. The Detector System

An illustration of a 3-D position-sensitive CZT detector is shown in Fig. 1. The CZT detector used in this study is 1.5 cm thick and its volume is $2.0\ \text{cm} \times 2.0\ \text{cm} \times 1.5\ \text{cm}$. The cathode is a simple continuous plane, while the anode consists of an array of 11×11 pixels. Each $1.22\ \text{mm} \times 1.22\ \text{mm}$ pixel is surrounded by a grid biased at a voltage lower than the pixel. This technique effectively steers electrons toward pixels, thereby improving charge-collection efficiency. Alternatively, the grid can be biased at the same potential as the anode pixels, i.e., 0 V. In this case, some charge will be collected by the grid if the electron cloud occurs outside of the pixel. The grid also serves as a guard ring to reduce the surface leakage current from the side of the crystal. The steering grid is 100 μm wide and has a 200 μm gap to the pixels. Therefore, the total pixel pitch is 1.72 mm. In this study, a prototype digital readout system was build, which is capable of digitizing preamplifier signals waveforms as a function of time from a 3×3 pixel array. These signals can be used to retrieve a wealth of information of the interaction, including sub-pixel interaction positions. The details of this system are given in Section VI-A.

III. System Modeling

A simulation was performed to find expected preamplifier output pulse waveforms. These simulated waveform results are then be used to develop and optimize the sub-pixel position estimation techniques for experimental data. The simulation package includes two components: charge transport and induction and electronic noise.

A. The Signal Induction

Charge induction on a given electrode can be calculated using the Shockley-Ramo theorem [11]. Barrett *et al.* showed an example to calculate the charge induction on electrodes [12]. Kim [10] described in detail a simulation procedure applied for pixelated CdZnTe detectors. This article uses a similar simulation method as Kim. In the following paragraphs, we will give a simple description of the method.

The track and velocity of electrons and holes are determined by modeling the operating electric field in the detector. It is assumed that electrons and holes are following electric field in the crystal bulk. When the charge reach electrode surface, holes are just simply collected by cathode. However, for electrons there are two boundary conditions defined to describe their behavior at anode surface based on grid bias. If grid is biased, we will assume full charge collection. Electrons that reach the gap instead of pixel pads or grid will be further transported along the electric field between grid and pixels on the anode surface; If grid is unbiased, electrons will stay in the location where they reach the anode surface.

The induced charge on each electrode is calculated from the weighting potential along each charge track. The final induced signal at time t is then equal to the product of the charge quantity and the difference in weighting potential between the charge carriers position at time t and its initial position. The operating and weighting fields are complicated in a pixelated detector. This problem is solved numerically using an electromagnetic field calculation software: *Maxwell v11* from Ansoft.

Fig. 2 gives an example of the simulated waveform signal induced on a center collecting pixel as well as the pixels that surround it. In this example, each electron cloud is modeled as a geometrical point with a total charge equivalent to the energy deposition of a 662-keV photon. Two electron clouds are simulated in this figure, one is located at the center of the collecting pixel (thick line) and another is near the pixel edge (dashed line). They are both in the middle depth of the detector. For this simulation, the cathode bias is -3000 V. Because the mobility of holes is much lower than that of electrons, only the electron drift was simulated during the charge collection time. The trapping of electrons in the detector is not modeled because it is not a critical factor in this study as will be discussed in Section V.

The signal induced on the center collecting pixel is very small in the detector bulk until the electron cloud drifts to the vicinity of the pixelated anode. In this anode region, the induced signal rises rapidly because of the large gradients in weighting potential and eventually, it will rise to an amplitude close to the original 662 keV. There is a small amplitude deficit due to the trapped holes in the detector bulk. Additionally, electron trapping can contribute to the deficit of the induced signal amplitude.

For the non-collecting neighboring pixels, the signals first rise as the electron cloud travels from the detector bulk to near the anode surface and then drop when the electron cloud enters the anode region. The boundary of the anode region is defined as

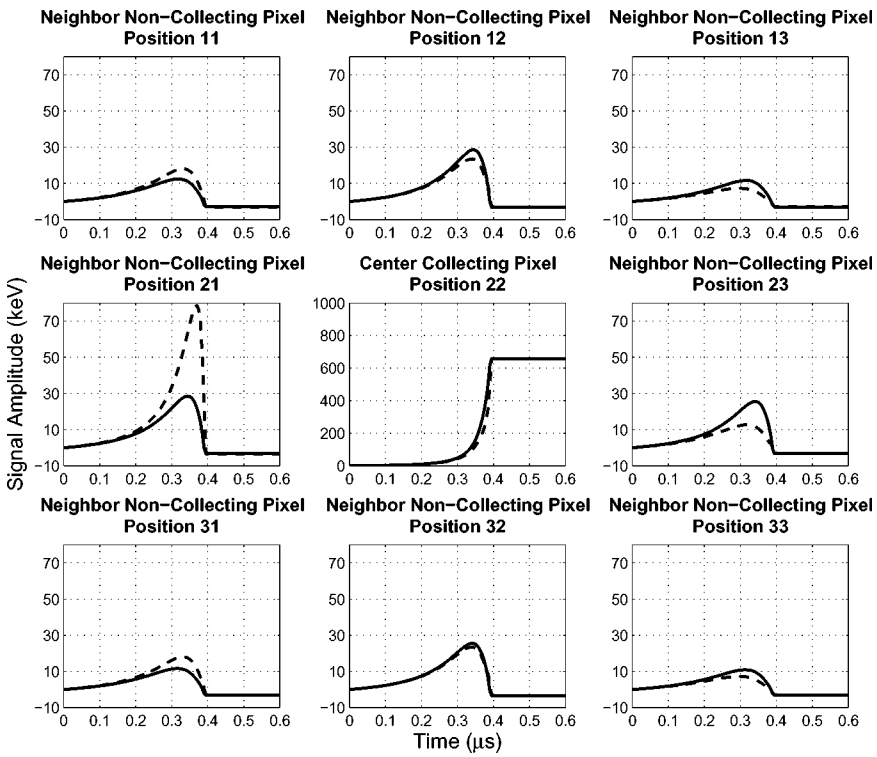

Fig. 2. Signal induction for a collecting pixel (pixel 22) and its 8 neighbors. The responses correspond to a single simulated 662-keV point electron cloud collected by the center pixel. The transient signals of the neighbor pixels are shown for two events: one happened underneath the center (thick line) and the other near the edge (dashed line) of the collecting pixel and close to pixel 21. They are both located in the middle depth of the detector.

the depth where the maximum of this "transient signal" happens, roughly one pixel size away from the anode surface. Eventually, the signals will drop to zero or to a negative value (hereafter referred as a "negative tail") due to the trapped holes. The amplitude of the negative tail depends on the depth of the initial interaction. When the interaction happens at the cathode surface, the neighboring pixel signal will drop to zero. If the interaction is in the detector bulk or the anode region, the negative tail occurs. The negative tail is the biggest if the interaction happens at the anode region boundary.

The peak signal amplitude of the neighboring pixel's transient waveform is very sensitive to the lateral position (or sub-pixel position) of the interaction position. As seen in Fig. 2, the induced signal on the neighboring pixels changes significantly from the thick line to the dashed line when the electron cloud moves from the pixel center to the edge. The reason is that when a transient signal reaches its maximum the distance between the electron cloud and a neighboring pixel depends significantly on lateral interaction position. As was mentioned earlier, the transient signal reaches its maximum when the electron cloud is roughly one pixel length away from the anode. At this time, the lateral distance from the electron cloud to the center of a neighboring pixel ranges from half a pixel to one-and-a-half pixels for interaction location on one edge of the charge collecting pixel or the other. As a result, the total 3-D distance from the electron cloud to a neighboring pixel at the transient peaking time strongly depends on the lateral position of the electron cloud at that time. Therefore, the peak amplitude of the neighboring transient signals actually gives the lateral position where the electron cloud enters the anode region.

An interaction location is the start point of an electron cloud trajectory. if an electron cloud trajectory is a straight line perpendicular to the cathode and anode surface, the neighboring transient signal peak amplitudes would be directly related to the initial lateral interaction position. However, the electron cloud trajectory can be bent because of grid bias or material defects. The impacts of those factors on neighboring pixel transient signals are different. The grid bias is used to help improve charge collection efficiency and it is normally very small comparing to the cathode bias. Its impact on an electron cloud trajectory is negligible before the electron cloud gets very close to the anode surface, so the initial interaction position can still be obtained by the neighboring transient signals. As for material defects, it can alter an electron cloud trajectory significantly when the electron cloud is still in the detector bulk. In this case, the neighboring pixel transient signals won't be able to provide initial interaction positions.

If a detector crystal has very good quality and is free of defects, we can use the peak amplitude of the transient signals to determine the sub-pixel position of an interaction. However, as we can see in Fig. 2, the transient signals are very fast and have very small amplitude compared to the charge collection signal. Electronic noise is expected to be the limiting factor in how accurately we can determine the sub-pixel interaction position.

B. Electronic Noise Simulation

Pullia and Riboldi [13] provide a method to precisely simulate the electronic noise of a detector system in the time domain. Simulation of the parallel and serial noise in our detector system is based on experimental data. The $1/f$ noise, is assumed

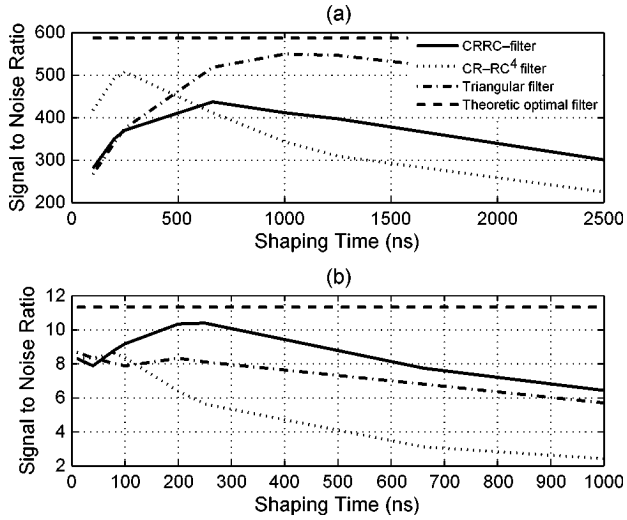

Fig. 3. The signal-to-noise ratio of different shaping filters for: (a) the charge-collecting pixel signal, and (b) the non-collecting pixel transient signal.

to be negligible for our first-order approximation. In this case, the noise parameters that need to be constructed for the noise model are the parallel- and serial-noise amplitudes, which are assigned to a and b respectively. The noise density function can be written as

$$S^2 = a^2 + b^2/\omega^2. \tag{1}$$

Where S^2 is in unit of $\mathrm{keV}^2/\mathrm{Hz}$ and ω is the circular frequency. To measure a and b, we can apply a $\mathrm{CR-RC}^4$ filter to the signal waveform and search for the lowest noise amplitude V_n and the corresponding shaping time τ_{opt}. The noise amplitudes can then be calculated as

$$\begin{aligned} a^2 &= V_n^2 \times \tau_{opt} \times C_1 \\ b^2 &= V_n^2/\tau_{opt} \times C_2, \end{aligned} \tag{2}$$

where C_1 and C_2 are the coefficients calculated from the response function of the filter. For a $\mathrm{CR-RC}^4$ filter, C_1 and C_2 are 220 and 31.4 respectively. If a different filter is applied, C_1 and C_2 would have different values. The near-optimal shaping time of a $\mathrm{CR-RC}^4$ filter for the collecting pixel signal was measured to be about 250 ns (at a peaking time of 1 μs) and the noise FWHM was 4 keV. With these parameters, a general noise model can be constructed for the waveform model.

C. Digital Filter Design

To compare the performance of estimating the transient signal amplitude on neighboring anode pixels, several digital filters, including CR-RC, triangular, and the theoretical optimal filter, were studied. The theoretical optimal filter is obtained based on the method described by Radeka [14]. For collecting pixels, the signal-to-noise ratio of the optimal filter is shown in Fig. 3(a). However, the optimal filter formula described in [14] cannot be directly applied to the neighboring transient signal. In [14], the signal amplitude is chosen to be the maximum value of the filtered signal. However, as will be discussed in Section IV, it is the difference between the maximum and minimum value of the filtered transient signal that provides a useful transient signal amplitude. In this case, the signal amplitude for transient signals can be written as

$$\begin{aligned} v_o &= v_o(t_{max}) - v_o(t_{min}) \\ &= \frac{1}{2\pi}\int_{-\infty}^{\infty} H(\omega)V_i(\omega)(e^{j\omega t_{max}} - e^{j\omega t_{min}})d\omega. \end{aligned} \tag{3}$$

Here, $v_o(t_{max})$ and $v_o(t_{min})$ are the signal maximum and minimum. $H(\omega)$ is the Fourier transform of the filter and $V_i(\omega)$ is the Fourier transform of the noise-free transient signal profile (or the mean input signal). If we know the noise power density function $S_i(\omega)$, the noise amplitude can be calculated as

$$V_n^2 = \frac{1}{2\pi}\int_{-\infty}^{\infty} |H(\omega)|^2 S_i(\omega)d\omega \tag{4}$$

The signal to noise ratio can then be expressed as

$$\eta^2 = \frac{v_o^2}{V_n^2} = \frac{\left|\int_{-\infty}^{\infty} H(\omega)V_i(\omega)(e^{j\omega t_{max}} - e^{j\omega t_{min}})d\omega\right|^2}{2\pi\int_{-\infty}^{\infty} |H(\omega)|^2 S_i(\omega)d\omega}, \tag{5}$$

The optimal signal-to-noise ratio [14] occurs when the frequency response of the filter is

$$\begin{aligned} H(\omega) &= k\frac{V_i^*(\omega)}{S_i(\omega)}(e^{-j\omega t_{max}} - e^{-j\omega t_{min}}) \\ &= k\frac{V_i^*(\omega)}{S_i(\omega)}e^{-j\omega t_{max}}\left[1 - e^{-j\omega(t_{min}-t_{max})}\right]. \end{aligned} \tag{6}$$

$V_i^*(\omega)$ is the conjugate of the Fourier transform of the input signal, k is a constant, and $e^{-j\omega t_{max}}$ is a time-shift term. Neither k nor $e^{-j\omega t_{max}}$ affect the signal-to-noise ratio, thus, they can be eliminated to simplify the equations. Hence, the optimal filter for neighboring pixel signals is

$$H_{opt}^{nb}(\omega) = \frac{V_i^*(\omega)}{S_i(\omega)}\left[1 - e^{-j\omega(t_{min}-t_{max})}\right]. \tag{7}$$

The time interval between occurrence of the maximum and minimum signal amplitude of the shaped transient signal depends on the digital filter. As a result, it is difficult to analytically derive the solution for an optimal filter. However, a solution can be found numerically by searching through all possible time intervals. The dashed line in Fig. 3(b) gives the signal-to-noise ratio of the optimal filters for simulated neighbor transient signals. The best signal-to-noise ratio can only be achieved with the optimal filter. As Fig. 3(b) shows, the CR-RC filter performs better than the other three filters and its best signal-to-noise ratio at the shaping time of 200 ns is very close to the optimal filter. Because the transient signal pulse waveform is a sensitive function of the 3-D position of interactions, it is very difficult to apply the optimal filter to calculate the sub-pixel position experimentally.

Therefore, we use a CR-RC filter for the transient signal filter as a good practical approximation. Based on the results in Fig. 3(b), it is possible to achieve position resolution similar to what can be obtained using the optimal filter.

IV. Sub-Pixel Position Calculation Algorithm

The maximum amplitude of the transient signals of the 8 neighboring pixels can be compared quantitatively to determine the sub-pixel position of an interaction. However, the transient signal maximum decreases as the interaction position changes from the cathode side toward the anode side. The signal becomes very small when the interaction is in the anode region. If we choose the signal maximum to calculate the sub-pixel position, the algorithm coefficients may vary from depth to depth and the sub-pixel position resolution will be poor in the anode region.

Fortunately, the signal maximum occurs in a certain depth for the interactions located at a particular lateral position, where the electron cloud just drifts past the boundary of the anode region. The weighting-potential change from this depth to the anode surface (charge fully collected) is independent of the initial depth of the electron cloud when this interaction occurs in the detector bulk. In other words, the signal difference between the signal maximum and its negative tail, the signal minimum, is not a function of interaction depth at a particular lateral position and in detector bulk. Therefore, we define the transient signal amplitude as the value difference between the signal maximum and minimum amplitudes. In the anode region this transient signal amplitude is no longer independent of interaction depth. However, it is still much bigger than the transient signal maximum, which is actually zero and thus this definition extends the active region where we can perform subpixel position calculation.

Transient signal amplitude is the key measurable parameter that is used to calculate sub-pixel interaction position. A method referred to as the *opposing-neighboring ratio* uses these neighbor pixel amplitudes to calculate the sub-pixel centroid position of an electron cloud. If the position of the center collection pixel and its 8 neighbors is labeled as shown in Fig. 2, the opposing-neighboring ratio along the lateral x direction, Rn_x can be written as

$$Rn_x(x,y,z) = \frac{s_{21}(x,y,z) - s_{23}(x,y,z)}{s_{21}(x,y,z) + s_{23}(x,y,z)}, \tag{8}$$

where $s_{21}(x,y,z)$ and $s_{23}(x,y,z)$ are the transient signal amplitudes on the middle-left and the middle-right neighbors respectively induced by an electron cloud located at (x,y,z). As described above, the transient signal amplitude is not a function of depth z unless the interaction happens in the anode region. Therefore, (8) can be simplified as

$$Rn_x(x,y) = \frac{s_{21}(x,y) - s_{23}(x,y)}{s_{21}(x,y) + s_{23}(x,y)}. \tag{9}$$

Here, Rn_x is not only a function of the lateral x coordinate of the electron cloud, but also the lateral y coordinate. If a electron cloud is moving along the y direction, its distance to the middle-left neighbor (pixel 21) and middle-right neighbor (pixel 23) will change, resulting in different induced signals on those neighbors. However, if the left three neighbors and right three neighbors are considered as a whole respectively, the mean distance from the moving electron cloud to these neighbors will change much less. Therefore, a new signal ratio can be written as

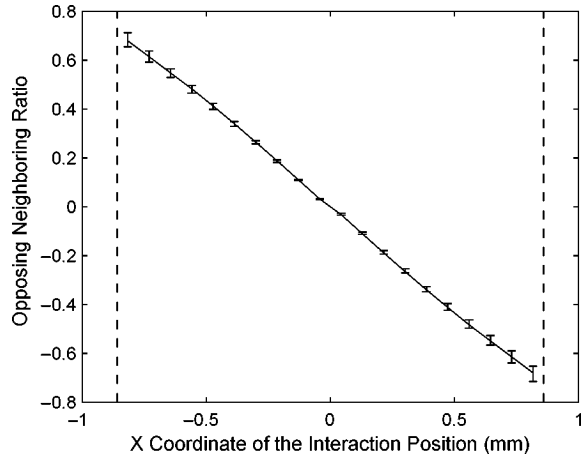

Fig. 4. The relationship between the opposing-neighboring ratio R_x and real lateral x coordination calculated by simulation. The curve gives R_x as a function of x when the electron cloud is in the middle of a pixel ($y = 0$) and near the cathode surface ($z = 0$). The error bars mark the range of the R_x if the lateral y position and the depth z of the electron cloud change in the pixel volume. The dashed lines mark the boundary of a pixel.

$$\begin{aligned} s_l(x) &\approx s_l(x,y) = s_{11}(x,y) + s_{21}(x,y) + s_{31}(x,y) \\ s_r(x) &\approx s_r(x,y) = s_{13}(x,y) + s_{23}(x,y) + s_{33}(x,y) \\ R_x(x) &= \frac{s_l(x) - s_r(x)}{s_l(x) + s_r(x)}. \end{aligned} \tag{10}$$

We call this the opposing-neighboring ratio. The relationship between R_x and the x coordinates is calculated by simulation for different lateral y positions and depths z. The result is presented in Fig. 4. The change in R_x due to the variation of the lateral y position and the depth z of an interaction is given by the error bar. As can be seen, such change is small compared to the pixel size, indicating that the approximation of (10) is valid. Additionally, Fig. 4 shows that the R_x versus x curve is close to a straight line. To a first order approximation, we can employ a linear function to model the signal ratio R_x versus x in the sub-pixel position calculation.

In the y direction, the opposing-neighboring ratio R_y can be formed the same way as for R_x:

$$\begin{aligned} s_t(y) &\approx s_t(x,y) = s_{11}(x,y) + s_{12}(x,y) + s_{13}(x,y) \\ s_b(y) &\approx s_b(x,y) = s_{31}(x,y) + s_{32}(x,y) + s_{33}(x,y) \\ R_y(y) &= \frac{s_t(y) - s_b(y)}{s_t(y) + s_b(y)}. \end{aligned} \tag{11}$$

Besides the opposing-neighboring ratio, there are at least two more ratios that can be used to calculate the electron cloud position:

1) the ratio between the neighboring pixel signals and the center pixel signal
2) the signal ratio between two corner neighbors and the center pixel signal.

We refer to (1) as the *neighbor-to-center ratio*, and (2) the *corner-neighbor ratio*. The neighbor to center ratio (Rc_x and

Rc_y) and corner neighbor ratio (Rcr_x and Rcr_y) are expressed as

$$Rc_x(x) = \frac{s_l(x)}{s_{22}}$$
$$Rc_y(y) = \frac{s_t(y)}{s_{22}} \tag{12}$$

and

$$Rcr_x(x,y) = \frac{s_{11}(x,y) - s_{13}(x,y)}{s_{22}}$$
$$Rcr_y(x,y) = \frac{s_{11}(x,y) - s_{31}(x,y)}{s_{22}} \tag{13}$$

where s_{22} is the charge collected by the center pixel. These two methods have their shortcomings. For the neighbor-to-center ratio, the ratio is not a linear function of the actual electron cloud position. For the corner-neighbor ratio, the ratio is a function of both x and y coordinates and thus is difficult to calibrate. Therefore, the opposing neighbors' transient ratio is preferred.

However, neighbor-to-center ratio and corner-neighbor ratio require fewer neighboring pixel signals than the opposing-neighboring ratio. The neighbor-to-center ratio requires three neighbors on one side of a collecting pixel. The corner-neighbor ratio method requires two corner neighbors. For multi-pixel interaction events, the induced signal on a neighboring pixel from a electron cloud may be polluted by the signal induction from another separate electron cloud. In this situation, opposing-neighboring ratio may not be applicable and then the neighbor-to-center ratio or corner-neighbor ratio could be employed to determine the sub-pixel position for each electron cloud. Section VII addresses this scenario in greater detail.

V. Estimate of Sub-Pixel Position Resolution by Simulation

The precision of the sub-pixel position obtained by the opposing-neighboring ratio method can be estimated based on the system model discussed in Section III. The results are given in Fig. 5. In this simulation, the energy deposition of the gamma ray is set to be 662 keV and the electronic noise is set to 4 keV FWHM. The cathode is assumed to be biased at -3000 V and the grid is at -100 V. The sampling frequency is set as 100 MHz. The energy is assumed to be deposited at a single space point rather than a extended electron cloud for principle study. Fig. 5(a) gives the bias of the calculated position using the linear-relation assumption of R_x (as defined in (10)) versus x from the true energy-deposition position. Fig. 5(b) presents the calculated sub-pixel position uncertainty due to the 4 keV electronic noise. The calculated position bias is smaller than the position uncertainty, indicating that the linear assumption is an appropriate model.

The dominant source of uncertainty in the calculated sub-pixel position is the electronic noise. Uncertainty in the collected charge due to charge production in the ionization process and charge trapping will generate proportional changes to the signals induced on all 8 neighbors. As a result, the associated fluctuation cancel out using the signal ratio. As seen in Fig. 5(b), the expected sub-pixel position resolution at 662 keV is below

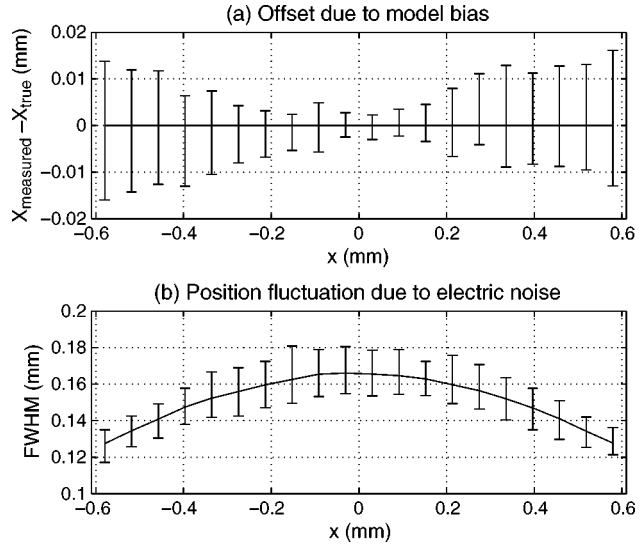

Fig. 5. Sub-pixel simulation performance results: (a) the offset difference between the mean calculated position and the true simulated position based on the linear assumption, and (b) the position variation in terms of FWHM due to 4 keV electronic noise. The offset and position variation is plotted for the x coordinate. The error bars mark the offset and FWHM range as the electron cloud position is shifted along y and z directions through the volume of the collecting-pixel column.

180 μm. This simulation result assumes energy is deposited at a single point. In reality, energy is deposited in an extended electron cloud. The calculated sub-pixel position for a real interaction is the centroid of the electron cloud. As a result, the size of the electron cloud will introduce additional uncertainty in the determination of the interaction position.

VI. Experimental Measurements and Analysis

A. Measured Sub-Pixel Position Resolution With Collimator

Results from a collimation experiment provide an experimental measure of the sub-pixel position resolution. Fig. 6 illustrates the design of the collimator experiment. The collimator is made of 6-cm thick tungsten with a 100-μm opening, separated by 3 cm away the bottom surface of the detector. The opening of the collimator is aligned parallel with the edge of a target pixel. A ^{137}Cs point source is placed in the collimator and used to irradiate a narrow section of the pixel from the cathode side of the detector. The irradiated pixel and its 8 neighbors are connected to eV-Products model 5093 preamplifiers. Each preamplifier signal is fed into a channel of a GaGe Octopus CompuScope model 8389 multichannel digitizer card (8 channels per card, 14-bit resolution, 125 MHz), operating at a 100 MSa/s sampling rate (10-ns sampling interval).

The detector is manufactured by eV-Products. The detector schematics are identical to those found in the system model discussion in Section III. During operation, the cathode is biased at -3000 V but the grid was unintentionally left unbiased. However the different grid bias shouldn't impact the conclusion we have achieved in the simulation.

The collimator is positioned near the center of the pixel at first and then moved toward the edge with a step size of 100 μm. For each collimator position, photopeak events from single-pixel interactions are selected for use in the sub-pixel study. For

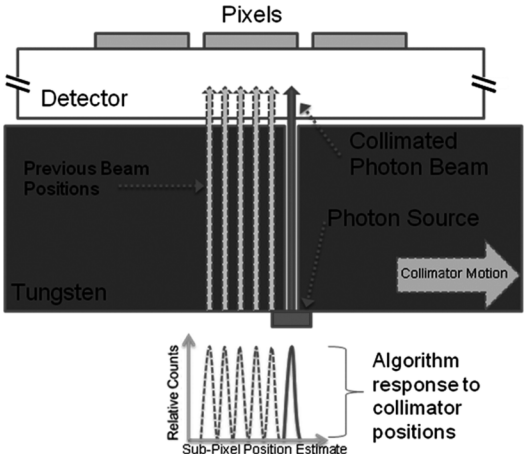

Fig. 6. The collimator design for experimentally measuring sub-pixel position resolution.

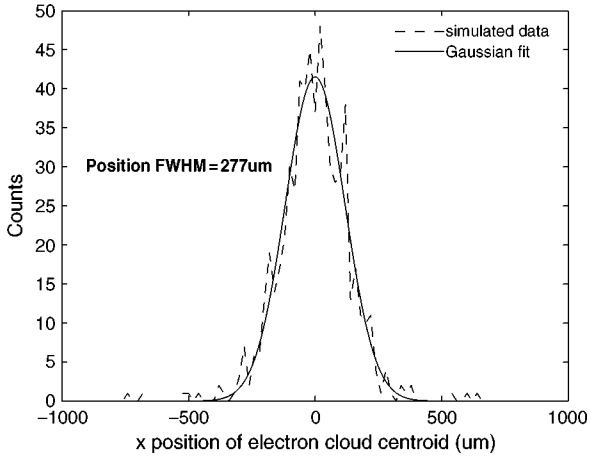

Fig. 8. The simulated distribution of the electron cloud centroid from a 662-keV gamma-ray source using a collimator. Distribution width is due to the collimator and electron cloud size.

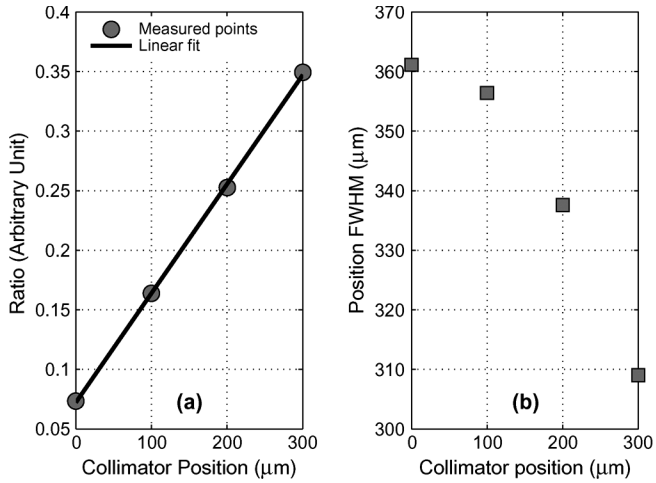

Fig. 7. Measured sub-pixel resolution at 662 keV: (a) the mean neighboring pixel ratio for each collimator position. This data is fitted by a linear function and the result shows the slope as $(9.2 \pm 0.5) \times 10^{-4}$ and the interception as 0.072 ± 0.009 with 95% confidence; (b) the FWHM of the position variance at each collimator position. The origin of x axis of these plots are the start location of the collimator instead of the center of the pixel.

neighbor-pixel signals, a CR-RC filter with 200-ns shaping time is employed. This filter choice is based on the simulation results described in Section III-C. The results of the measurements at four collimator positions are summarized in Fig. 7. Fig. 7(a) shows the opposing-neighboring ratio for each collimator position and Fig. 7(b) gives the measured position uncertainty. The x axis origin of both plots are the start location of the collimator. The FWHM of the position estimate is below 360 μm.

However, this 360-μm position uncertainty is not equivalent to the sub-pixel resolution. There are two more factors that add uncertainty to the measurement: (1) collimator-beam size and (2) electron cloud size. The collimator has a 100-μm opening, but the beam will be spread bigger at the detector surface and the beam size will become even wider when the interactions occur at deeper depths in the detector. The increase in measured resolution caused by the collimator is significant. Additionally, the measured sub-pixel position of each interaction represents the centroid of the ionized electron cloud not the initial gamma-ray interaction position. As a result, even when the gamma beam is fixed at a single position relative to the detector, the electron cloud centroid will be different if the secondary fast electron follows a different track. Using the Geant4 simulation package, we can simulate the total uncertainty contribution from the two factors together. As shown in Fig. 8, we find that the collimator beam and 662-keV electron cloud can cause 280-μm FWHM position uncertainty in the measurement. The contributions of spreading from collimator and electron cloud size can be simulated individually and the result shows collimator can cause 150 μm spreading in FWHM and electron cloud size introduces 240 μm. Though both collimator and electron cloud caused spreading are not strictly Gaussian shaped, the quadratic sum of the contribution from collimator and electron cloud results in the same result as obtained with the simulation considering them together, indicating quadratic operation can be applied in estimating the contribution of each factor to sub-pixel position resolution measurement.

After quadratic subtraction, the real sub-pixel resolution of the system in terms of determining electron cloud centroid position is calculated to be around 230 μm at 662 keV. However, if we consider the initial gamma-ray interaction position, we would need to add the the additionally uncertainty caused by electron cloud size. The projection of electron cloud size on x-y plane is a function of recoil electron direction, especially at high energy. If assuming the secondary electrons are emitted isotropically, the sub-pixel position resolution of initial gamma-ray interaction position would be 330 μm FWHM at 662 keV.

The 230-μm sub-pixel position resolution at 662 keV is a little bit worse than the simulation result of 180 μm. There are several factors that may cause the difference, including the inaccuracy of the measured geometry of the collimator setup (especially the distance between the detector and the collimator and the opening width), slight skewing of the collimator beam, the neglected $1/f$ noise, the diffusion of the electron cloud and material defects.

The inaccuracy of the measurement on geometry setup can be estimated in a easy way. The spreading caused by the collimator should be proportional to $\delta \times (d+z)/z$, where δ is the

opening width, d is the distance between collimator surface and detector surface and z is the collimator thickness. It can be calculated that even with 1 cm error on d or z, the change of total uncertainty caused by collimator and electron cloud would be smaller than 20 μm. For opening width δ, the error of measurement should be less than 10% and its influence on total uncertainty can be calculated to be smaller than 20 μm too. Therefore, the geometry measurement error should be negligible. Diffusion can change the drifting path of electrons [15]. For our 1.5 cm CdZnTe crystals at 3000 V, diffusion caused position uncertainty for each electron would be about 70 μm in standard deviation and thus 170 μm in FWHM if assuming Gaussian distribution. However, ideally diffusion shouldn't shift the centroid of an electric cloud if the electron cloud is consisted of infinite number of electrons. In reality we expect additional uncertainty from diffusion but its impact on sub-pixel position resolution should be much smaller than 170 μm and we expect its impact on the measurement uncertainty should be negligible. The presence of $1/f$ noise may change the performance of the CR-RC filter and cause some underestimation of the uncertainty from the electronic noise in simulation. At last, the material defects in CdZnTe has been known for deviate electrons from drifting straight [16]. In a poor crystal, this effect can move electron several hundred microns in lateral direction. In our experiment, a good CdZnTe detector was chosen but the deviation should still be noticeable according to Kaye *et al.* [16]. Therefore, we suspect material defects to be the main cause of the slight inaccuracy of the collimator experiment result.

The sub-pixel position resolution of electron cloud centroid is proportional to the energy deposition. The reason is the induced signals on the neighboring pixels are proportional to the energy deposition while the electronic noise is a constant. However, with the energy deposition increases, the electron cloud size gets larger. The total influence of those two effects will make the measured gamma-ray interaction position resolution improve at first with energy deposition increasing and then degrade when the energy deposition passes a favorite energy. On the other hand when the energy of recoil electrons is very high, the electron track would be very long and there might be a chance to extract the electron cloud distribution and reduce the impact of the large electron cloud size on identifying gamma-ray interaction position.

B. Complete Charge Collection Boundary

If a source is placed on the detector's cathode side and far from the detector, the single-pixel photopeak counts should be distributed uniformly along the lateral plane of the collecting pixel.

The boundary of this distribution marks the edge of the complete charge collection region. If the steering grid between the pixels is biased at the correct voltage, the electrons are expected to be steered toward the pixel and no charge should be lost in the gap between anode electrodes. In this case, the full pixel is the complete charge collection region and photopeak counts distribution should spread from one pixel edge to another, namely from -0.86 mm to 0.86 mm since the pixel pitch is 1.72 mm. When the grid is unbiased or grounded, only those events located under the pixel pad can be fully collected. The complete charge collection region should shrink to the pixel pad size, which is 1.22 mm.

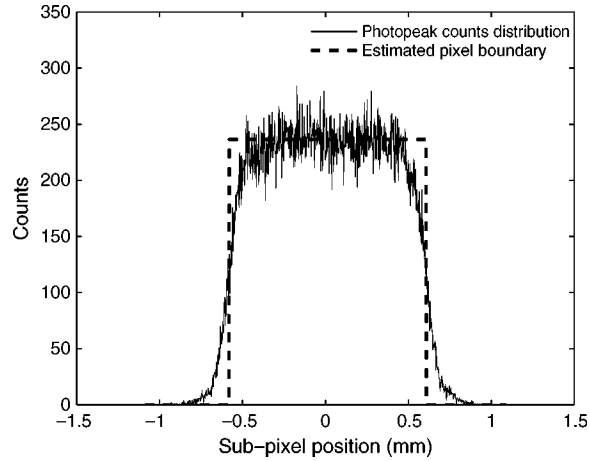

Fig. 9. The distribution of single-pixel photopeak events inside a pixel.

Fig. 9 shows the distribution of measured single-pixel photopeak events within a pixel when the steering grid is unbiased. The dotted line marks the measured pixel boundary of complete charge collection. As shown, the complete charge collection region is from -0.6 mm to 0.6 mm, totally 1.2 mm, consistent with our expectation.

The pixel boundary can affect the measured result of the collimator position. When the collimator is placed close to the complete charge collection boundary with unbiased grid, a portion of events will lose some charge to the gap or the grid and then they will not be registered as photopeak events. If we only choose photopeak events to measure the collimator center position, the measured collimator center position will be shifted. Fig. 10 shows that the center position of the selected photopeak events, or the measured collimator center, is shifted toward the inside of the pixel when the collimator is placed near the edge of the complete charge collection region. The dotted line shows the edge of the complete charge collection region. A simulation was carried out to test this behavior. The result is also shown in Fig. 10. The solid curve gives the calculated collimator center using only photopeak events based on the sub-pixel calculation algorithm. It agrees well with the measurement.

VII. Sub-Pixel Resolution for Two-Pixel Events

Two-pixel events can be categorized into three groups according to the distance between the two triggering pixels:

1) neighboring events, including side neighboring or diagonally neighboring events
2) non-neighboring events with a pixel-center-to-pixel-center distance less than three pixels, and
3) non-neighboring events with a pixel-center-to-pixel-center distance greater than or equal to three pixels.

In the discussion above, we only considered the induced signals on the 8 pixels surrounding the charge collecting pixel. For the non-neighboring pixels, the distance to the electron cloud is far, but signals are still induced. However, these signals are so small that we can ignore them in a first order approximation. With

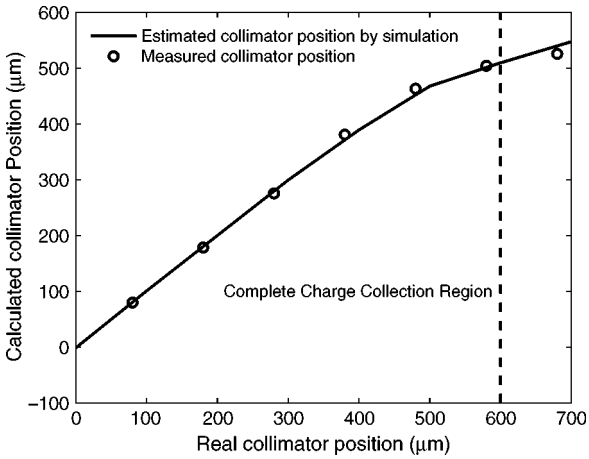

Fig. 10. Calculated position versus collimator position including a comparison between the simulation and experimental results. The dotted line marks the boundary of the complete charge collection region.

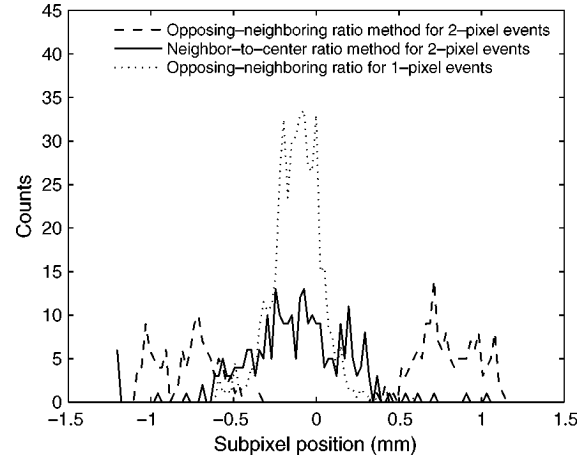

Fig. 12. Sub-pixel position for the two-pixel events in the collimator experiment. The energy deposition on the neighboring pixels is required to be greater than 100 keV.

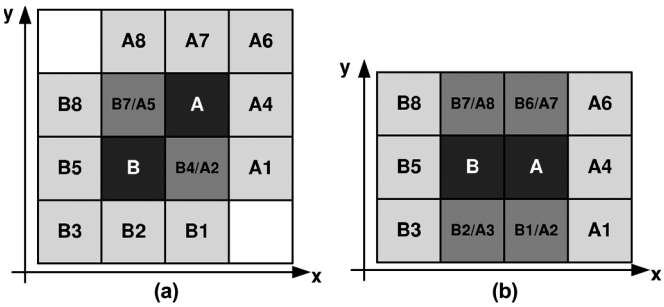

Fig. 11. The two cases of the arrangement of the triggered pixels for neighboring pixel events.

this assumption, the sub-pixel position calculation can be performed in the same way as it was for single-pixel events in case (3). However, for case (1) and case (2), the induced signal on a neighboring pixel from one electron cloud may be polluted by the induced signal from another electron cloud. To study these two cases, they can be further grouped into two categories based on the arrangement of the triggered pixels:

(a) the two collecting pixels are diagonally placed, and
(b) the two collecting pixels are both on the same row or column

Fig. 11 illustrates the two categories of neighboring pixel events. In Fig. 11(a), the two collecting pixels are pixel A and pixel B. The neighboring pixels of pixel A are labeled as A1, A2, A4, A5, A6, A7 and A8, while for pixel B as B1, B2, B3, B4, B5, B6, B7 and B8. Based on our assumption that the induced signals on non-neighboring pixels are negligible, the signals on the neighboring pixels except pixel B7/A5 and pixel B4/A2 are induced only by one electron cloud and their amplitudes can indicate the position of that electron cloud. These unpolluted neighbors are sufficient to apply neighbor-to-center ratio (as defined in Section IV) and both x and y sub-pixel positions can be determined.

For the case shown in Fig. 11(b), the x-direction unpolluted neighbors for collecting pixel A are A1, A4 and A6. They form one column so one can apply the neighbor-to-center ratio for x direction. However, for the y direction, there is not an entire row of 3 unpolluted pixels. Therefore, the corner neighbor ratio method needs to be employed. We will discuss the application of neighbor-to-center ratio first and then the corner-neighbor ratio.

As discussed in Section IV, the neighbor-to-center ratio does not have a linear relationship with the interaction position. However, the opposing-neighboring ratio is a linear function of interaction position. Therefore, we can associate the neighbor-to-center ratio with the opposing-neighbor ratio to calibrate the nonlinear relation. This step can be done for single-pixel events.

To demonstrate the effectiveness of the neighbor-to-center ratio, we again use a fan-beam collimator experiment. The collimator was placed near the center of a pixel and its opening was oriented along the y direction so that all the events through the collimator were located around $\mathrm{x} = 0$. The neighboring two-pixel photopeak events were chosen and the sub-pixel position of the first interaction (its electron cloud was collected by the collimated pixel) was calculated with the neighbor-to-center ratio. As a comparison, we also blindly applied the opposing-neighboring ratio method even though the neighboring pixel signals were polluted. If the sub-pixel position calculation was correct, we should observe the first interaction position around $\mathrm{x} = 0$.

The results are presented in Fig. 12. The sub-pixel position distribution for single-pixel photopeak events is also plotted to give a reference position of the collimator. As can be seen, the sub-pixel position calculated from the opposing-neighboring ratio is pushed away from the real interaction position. Since for neighboring two-pixel events, a neighbor is collecting charge and its total induced signal becomes much higher than it should be. The neighbor-to-center ratio method gives a much better result. However, the position resolution is poorer than that for the single-pixel events. A major reason is that the energy of each interaction of a two-pixel photopeak events is less than that of single-pixel photopeak events leading to smaller induced neighboring pixel signals. Additionally, the neighbor-to-center ratio for neighboring two-pixel events assumes the induced signals are negligible if the distance is greater than two pixels. However, the induced signals are not exactly zero. This small

charge induction can cause small offsets of the calculated interaction position from the real interaction position. This effect will be most prominent when the electronic noise becomes very low.

In Fig. 11(b), the y sub-pixel position needs to be calculated by the corner-neighbor ratio. As mentioned in Section IV, the corner-neighbor ratio is a function of both x and y coordinates. Thus, the x sub-pixel position needs to be calculated first by the center-to-neighbor ratio and then the corresponding relation of corner-neighbor ratio versus y position can be extracted and used for calculating the y sub-pixel position. As a result, the corner-neighbor ratio is expected to have higher uncertainty than the neighbor-to-center ratio.

VIII. Conclusion

The purpose of this article is to introduce and justify a sub-pixel calculation algorithm based on the digital readout of the induced signal on the charge collecting pixel and its 8 neighbors. Without such a method, the lateral position resolution of pixelated, 3-D position sensitive, CdZnTe detectors is limited by their pixel pitch. This barrier introduces a significant limitation on the Compton imaging angular resolution. To improve lateral position resolution to the sub-pixel scale, algorithms based on signals induced on pixels that neighbor a charge collecting pixel are used. The opposing-neighboring ratio method is shown to be capable of providing accurate estimates of sub-pixel electron cloud centroid position. A detailed system simulation predicted 180-μm FWHM position resolution at 662 keV with 4-keV electronic noise. A collimator experiment resulted in a 360 μm position fluctuation for a 662 keV ^{137}Cs source. After subtracting the uncertainty caused by the collimator beam width and the electron cloud size, the experimental sub-pixel position resolution for measuring the electron cloud centroid of a recoil electron is found to be about 230 μm. The uncertainty of measured gamma-ray interaction position would then be 330 μm at 662 keV if we assume the secondary electrons are emitted isotropically.

Besides the opposing-neighboring ratio, two additional methods (neighbor-to-center ratio and corner-neighbor ratio) are discussed for the more difficult case of multi-pixel charge collection events. It is demonstrated that neighbor-to-center ratio method is effective in estimating the sub-pixel interaction position for two-pixel events.

Acknowledgment

The authors would like to thank their colleague C. Wahl for helping edit this article.

References

[1] F. Zhang, W. R. Kaye, and Z. He, "Performance of 3-d position sensitive CdZnTe detectors for gamma-ray energies above 1 MeV," in *Proc. IEEE Nucl. Sci. Symp. Conf. Record (NSS/MIC)*, Orlando, FL, Oct. 2009, pp. 2012–2016.

[2] D. Xu, Z. He, C. E. Lehner, and F. Zhang, "4-pi compton imaging with single 3-D position sensitive CdZnTe detector," in *Proc. SPIE*, 2004, vol. 5540, pp. 144–155.

[3] W. K. Warburton, "An approach to sub-pixel spatial resolution in room temperature X-ray detector arrays with good energy resolution," in *Mater. Res. Symp. Proc.*, 1998, vol. 487, pp. 531–535.

[4] M. Burks, E. Jordan, E. Hull, L. Mihailescu, and K. Vetter, "Signal interpolation in germanium detectors for improved 3-D position resolution," in *Proc. IEEE Nucl. Sci. Symp. Conf. Record (NSS/MIC)*, Rome, Italy, Oct. 2004, pp. 309–394.

[5] C. S. Williams, W. P. Baker, L. W. Burggraf, P. E. Adamson, and J. C. Petrosky, "Toward simultaneous 2-D ACAR and 2-D DBAR: Sub-pixel spatial characterization of a segmented HPGe detector using transient charges," *IEEE Trans. Nucl. Sci.*, vol. 57, no. 2, pp. 860–869, Apr. 2010.

[6] D. Marks, H. Barber, H. Barrett, J. Tueller, and J. Woolfenden, "Improving performance of a CdZnTe imaging array by mapping the detector with gamma rays," *Nucl. Instr. Meth.*, vol. 428, no. 1, pp. 102–112, 1999.

[7] J. S. Vickersa and S. Chakrabarti, "Silicon-anode detector with integrated electronics for microchannel-plate imaging detectors," *Rev. Sci. Instr.*, vol. 70, no. 7, pp. 2912–2916, 1999.

[8] J. Jakubek and J. Uher, "Fast neutron detector based on TimePix pixel device with micrometer spatial resolution," in *Proc. IEEE Nucl. Sci. Symp. Conf. Record (NSS/MIC)*, Orlando, FL, Oct. 2009, pp. 1113–1116.

[9] T. Narita, J. E. Grindlay, J. Hong, and F. C. Niestemski, "Anode readout for pixellated CZT detector," in *Proc. SPIE*, 2004, vol. 5165, pp. 542–547.

[10] J. C. Kim, S. E. Anderson, W. Kaye, S. J. Kaye, Y. Zhu, F. Zhang, and Z. He, "Study on effect of charge sharing events in common-grid pixelated cdznte detectors," in *Proc. IEEE Nucl. Sci. Symp. Conf. Record (NSS/MIC)*, Orlando, FL, Oct. 2009, pp. 1640–1646.

[11] Z. He, "Review of the Shockley-Ramo theorem and its application in semiconductor gamma-ray detectors," *Nucl. Inst. Meth. A*, vol. 463, pp. 250–267, 2001.

[12] H. H. Barrett, J. D. Eskin, and H. B. Barber, "Charge transport in arrays of semiconductor gamma-ray detectors," *Phys. Rev. Lett.*, vol. 75, no. 1, pp. 156–159, 1995.

[13] A. Pullia and S. Riboldi, "Time-domain simulation of electronic noises," *IEEE Trans. Nucl. Sci.*, vol. 51, no. 4, pp. 1817–1822, Aug. 2004.

[14] V. Radeka, "Least-square-error amplitude measurement of pulse signals in presence of noise," *Nucl. Instr. Meth.*, vol. 52, no. 1, p. 86, 1967.

[15] G. F. Knoll, *Radiation Detection and Measurement*, 3rd ed. Hoboken, NJ: Wiley, 1999.

[16] S. Kaye, W. Kaye, and Z. He, "Experimental demonstration of coded aperture imaging using thick 3D-position-sensitive CdZnTe detectors," in *Proc. IEEE Nucl. Sci. Symp. Conf. Record (NSS/MIC)*, Orlando, FL, Oct. 2009, pp. 1902–1906.